Letter

Coupling x-ray photon correlation spectroscopy and dynamic coherent x-ray diffraction imaging: Particle motion analysis from nano-to-micrometer scale

Shuntaro Takazawa,[1,2,3] Duc-Anh Dao,[4] Masaki Abe,[1,2,3] Hideshi Uematsu,[1,2,3] Nozomu Ishiguro,[1,3,5] Taiki Hoshino,[1,3,5,*] Hieu Chi Dam,[1,4,†] and Yukio Takahashi[1,3,5,‡]

[1]*International Center for Synchrotron Radiation Innovation Smart (SRIS), Tohoku University, 2-1-1 Katahira, Aoba-ku, Sendai 980-8577, Japan*

[2]*Department of Metallurgy, Materials Science and Materials Processing, Graduate School of Engineering, Tohoku University, Aoba-yama 02, Aoba-ku, Sendai 980-8579, Japan*

[3]*RIKEN SPring-8 Center, 1-1-1 Kouto, Sayo-cho, Sayo-gun, Hyogo 679-5148, Japan*

[4]*Japan Advanced Institute of Science and Technology, Nomi, Ishikawa 923-1292, Japan*

[5]*Institute of Multidisciplinary Research for Advanced Materials (IMRAM), Tohoku University, 2-1-1 Katahira, Aoba-ku, Sendai 980-8577, Japan*

(Received 6 February 2023; revised 1 June 2023; accepted 6 October 2023; published 3 November 2023)

Two well-known measurement methods use coherent x rays: x-ray photon correlation spectroscopy (XPCS) and coherent x-ray diffraction imaging (CXDI). We propose and demonstrate an approach to analyze particle motion in heterogeneous solutions over a wide spatiotemporal scale by combining XPCS and dynamic CXDI using a data-driven approach. By applying this approach to analyze of the dynamics of colloidal gold particles dispersed in aqueous polyvinyl alcohol solutions, we found that Brownian motion exists in the range of a few hundred nanometers, and two modes of motion exist in the micrometer range, i.e., trapping in a narrow region and diffusion motion along a preferred direction. This approach can be applied to analyze dynamic heterogeneity in materials and cells that do not transmit visible light and electrons.

DOI: 10.1103/PhysRevResearch.5.L042019

The motion of particles inside liquids and solids is related to the mechanical properties of materials, e.g., the viscoelasticity of nanocomposites [1]. Particles are also used to probe the rheological properties within living cells [2]. In both cases, it is necessary to observe the particle motion over a broad spatiotemporal scale. Particle motion is analyzed either by examining the temporal correlation of scattered light intensity from particles or by direct observation. Both methods are extensively used in the visible light range and are commonly known as dynamic light scattering (DLS) [3] and single-particle tracking (SPT) [4]. The particle motion information obtained by DLS is the average of all the particles present in the illuminated area of the sample. SPT can only analyze particles within the field of view and depth of field of the microscope, which often limits the sample environment. However, the information obtained is differentiated for every particle in the illuminated area and can provide information on spatial motion inhomogeneity. Polymers and biological cells have complex internal structures, and particle diffusion is based on multiple modes of motion [5,6], thus necessitating a method for classifying the modes of motion. For example, classification methods based on multiple parameters related to particle motility have been investigated [7,8]. SPT in the visible light range makes it difficult to observe dynamic phenomena with spatial resolution at the nanoscale. It is also difficult to observe samples that do not transmit visible light. Using transmission electron microscopy, dynamic phenomena can be observed with single-nanometer spatial resolution [9], but it is difficult to observe micrometer-order thick samples.

X-rays, owing to their short wavelength and penetration power, are suitable for observing microscopic dynamic phenomena inside thick materials. X-ray photon correlation spectroscopy (XPCS) [10] can be regarded as a DLS method in the x-ray region and is used to analyze dynamic phenomena inside materials at the nanoscale based on the time correlation of coherent x-ray scattering intensities. The use of heterodyne XPCS [11] has also been proposed to analyze multiple motion modes, which requires the construction of a stable optical system with drift responses with smaller magnitudes than those of conventional XPCS [12]. Coherent x-ray diffraction imaging (CXDI) [13,14] is one of the methods used to obtain high spatial resolution images using x rays. The phase image of a sample is reconstructed by the phase-retrieval calculation of the two-dimensional coherent x-ray diffraction intensity pattern from the sample. Scanning CXDI [15], commonly known as x-ray ptychography, is extensively used in synchrotron radiation facilities; however, it has been challenging to capture the dynamic phenomena of samples in terms of temporal

*taiki.hoshino.c7@tohoku.ac.jp
†dam@jaist.ac.jp
‡ytakahashi@tohoku.ac.jp

Published by the American Physical Society under the terms of the Creative Commons Attribution 4.0 International license. Further distribution of this work must maintain attribution to the author(s) and the published article's title, journal citation, and DOI.

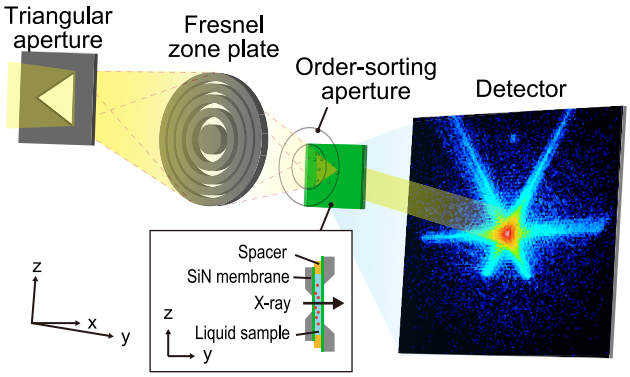

FIG. 1. Schematic of coherent diffraction pattern measurement of gold colloidal particles in solution.

resolution. Several nonscanning CXDI methods with excellent temporal resolution have been proposed [16–23]. However, these are still in the proof-of-principle stage, and there have been no reports capturing movement in actual samples in the hard x-ray region. Recently, we proposed and demonstrated a practical method for single-frame CXDI [24,25], in which a triangular aperture is used as a critical element in the optical system. The image of a selected field of view of an extended object is reconstructed from the single-frame diffraction intensity pattern based on a phase-retrieval calculation.

Herein, we first demonstrate the visualization of nanoscale dynamics by coupling XPCS and dynamic CXDI using synchrotron x rays. We employ several machine-learning techniques as a data-driven approach to perform SPT to extract and analyze the kinetics of individual particles. This approach enables us to investigate novel behaviors of nanoparticles at a large spatiotemporal scale by considering the phenomenon based on data analysis and obtaining statistical evidence to gain insights objectively that could lead to the proper reasoning of novel observations.

Figure 1 shows a conceptual diagram of the measurement performed at SPring-8 BL29XUL [26]. A 4.5 wt % polyvinyl alcohol (PVA) solution containing gold colloidal particles (particle size = 150 nm) was prepared. The PVA solution at 4.5 wt % is known as a Newtonian fluid according to the literature; thus, the diffusive behavior of particles should be in a simple Brownian manner [27]. Using the preparation volume, the concentration of colloidal gold particles in the PVA solution was estimated to be 0.74 wt %. The aqueous, gold colloid solution was then sealed in a cell made by sandwiching a Kapton spacer (thickness = 50 μm) between two silicon nitride membranes. The depth of focus [28] in the present CXDI system was estimated to be 138 μm, which is larger than the thickness of the Kapton spacer. The number of particles in the irradiated volume was estimated to be approximately 120, which is sufficient according to the previous studies using nanofocused beams [29,30]. The particles reached a state of sedimentation equilibrium after a certain time in this PVA solution, and all the synchrotron experiments were performed in the sedimentation equilibrium state. The incident 5-keV monochromatic x-ray beam was cut by a triangular aperture (side length of ∼10 μm); the triangular apertures were fabricated using focused ion beam processing on platinum foil (thickness = 15 μm, polished on both sides). The Fresnel zone plate (FZP) reduced the triangular aperture by a factor of 2, and a triangular x-ray beam of approximately 5 μm per side was illuminated onto the sample. The diffraction intensity patterns were recorded by using an in-vacuum pixelated detector (EIGER 1M, Dectris) with a pixel size of 75 μm, which was placed 3.14 m downstream of the sample. To suppress x-ray scattering from the air, the optical elements, the sample, and the detector were placed in a vacuum chamber and maintained at a pressure of ∼1 Pa. The number of photons incident on the sample surface was $\sim 3 \times 10^6$ photons/s. The temperature increases due to x-ray absorption into the solution were estimated to be less than 0.2 °C/s. As the solution conducts heat by convection, the effect of the temperature increase due to x-ray irradiation is negligible. Diffraction intensity patterns were collected using (a) 2000 consecutive images with an exposure time of 1 s and (b) 1000 consecutive images with an exposure time of 0.1 s. Under both conditions, x rays were illuminated at the same position on the sample.

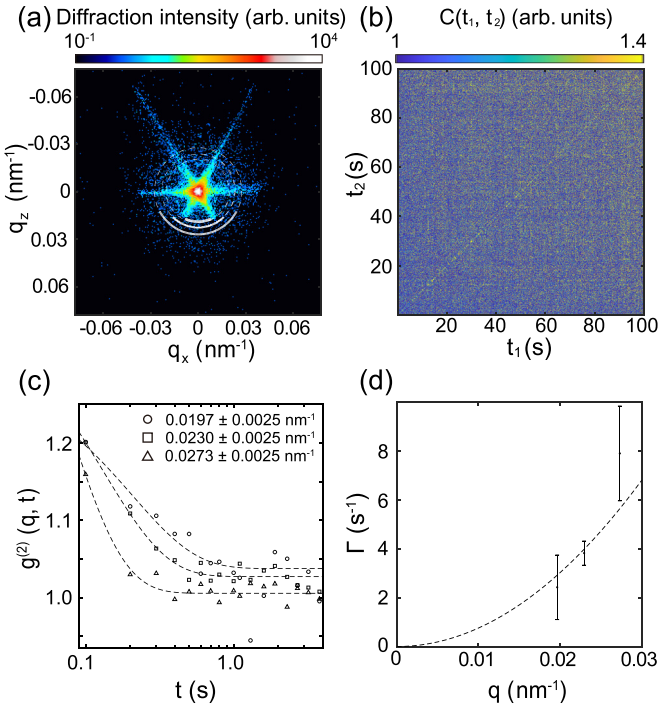

FIG. 2. (a) Diffraction pattern from an aqueous gold colloid solution measured with an exposure time of 0.1 s. (b) Two-time correlation calculated from the diffraction intensity in the region $q = 0.0230 \pm 0.0025$ nm^{-1}. (c) Time autocorrelation function normalized by the parameters obtained by curve fitting. (d) q dependence of the inverse of the relaxation time, $\Gamma(q)$. Error bars are standard deviations in curve fitting.

First, the fast dynamics of the particles were analyzed using XPCS. Figure 2(a) shows one of the diffraction pattern datasets measured at an exposure time of 0.1 s. The time autocorrelation function was calculated using the diffraction intensities at $|\mathbf{q}| = 0.0197$, 0.0230, and 0.0273 nm^{-1} outside the FZP projection region, shown using white lines in Fig. 2(a), where $\mathbf{q}$ is the scattering vector. Figure 2(b) shows a two-time correlation function [31] calculated from the

scattering intensity at $|\mathbf{q}| = 0.0230 \pm 0.0025\ \mathrm{nm}^{-1}$ using

$$C(q, t_1, t_2) = \frac{\langle I(\mathbf{q}, t_1) I(\mathbf{q}, t_2)\rangle_{\mathrm{pixel}}}{\langle I(\mathbf{q}, t_1)\rangle_{\mathrm{pixel}} \langle I(\mathbf{q}, t_2)\rangle_{\mathrm{pixel}}}, \tag{1}$$

where $I(\mathbf{q}, t_i)$ is the scattering intensity at $\mathbf{q}$, and time t_i $\langle\cdots\rangle_{\mathrm{pixel}}$ is the average of all pixels. It has been reported that radiation damage can cause the cross-linking of PVA polymers when present in an aqueous solution [32]. Because no correlation trend is observed in Fig. 2(b), the effect of the radiation damage of the PVA aqueous solution on the motion of colloidal gold particles is considered to be negligible. To obtain the relaxation time of the motion of gold colloidal particles, the temporal autocorrelation function $g^{(2)}(q, \tau)$ was calculated from the scattering intensity at $q = 0.0197 \pm 0.0025$, 0.0230 ± 0.0025, and 0.0273 ± 0.0025 nm^{-1} using

$$g^{(2)}(q, \tau) = \frac{\langle\langle I(\mathbf{q}, t) I(\mathbf{q}, t+\tau)\rangle_{\mathrm{pixel}}\rangle_t}{\langle\langle I(\mathbf{q}, t)\rangle_{\mathrm{pixel}}\rangle_t^2}, \tag{2}$$

where τ is the time interval between the two diffraction patterns for which the intensity correlation was calculated. Curve fitting was then performed with

$$g^{(2)}(q, \tau) = \beta(q)\exp\{-2\Gamma(q)\cdot\tau\} + g_\infty(q), \tag{3}$$

where $\beta(q)$ is the contrast, $\Gamma(q)$ is the inverse of the relaxation time, and g_∞ is the baseline. Figure 2(c) shows the autocorrelation and fitting curves [33]. If the mode of motion of colloidal gold particles in an aqueous solution is Brownian, the relationship between the inverse of the relaxation time and q is $\Gamma(q) = \mathrm{D}q^2$ [3], where D corresponds to the diffusion coefficient of colloidal gold particles in motion in the PVA solution. Figure 2(d) shows a plot of the inverse of the relaxation time $\Gamma(q)$ and a curve-fitting approximation of $\Gamma(q) = \mathrm{D}q^2$. Because the inverse of the relaxation time $\Gamma(q)$ shows a tendency to follow $\Gamma(q) \propto q^2$, the motion of particles in the illuminated region can be regarded as Brownian motion in a simple liquid with $D_{\mathrm{XPCS}} = 7550 \pm 850\ \mathrm{nm}^2/\mathrm{s}$. Additionally, in Fig. 2(c), the baseline increased with a decrease in q, possibly suggesting the presence of another slower mode on a larger spatial scale.

The slow motion of individual particles was then analyzed using real-space movies of single-frame CXDI. In image reconstruction, a single-object function $T_\mathbf{r}$ was reconstructed from a single diffraction pattern $I_\mathbf{q}$ using the probe function $P_\mathbf{r}^{(k)}$ with modes $k = 1$, 2, 3, and 4. The probe function was obtained using x-ray ptychography. Herein, we employed a phase-retrieval algorithm based on the reciprocal-space constraint expressed as

$$\psi_\mathbf{r}'^{(k)} = \mathcal{F}^{-1}\left[\sqrt{I_\mathbf{q}}\frac{\widetilde{\Psi}_\mathbf{q}^{(k)}}{\sqrt{\sum_k \left|\widetilde{\Psi}_\mathbf{q}^{(k)}\right|^2}}\right] \tag{4}$$

and the subsequent update in the real space given as

$$T_\mathbf{r}' = T_\mathbf{r} + \alpha\frac{\sum_k P_\mathbf{r}^{(k)*}\left\{\psi_\mathbf{r}'^{(k)} - \psi_\mathbf{r}^{(k)}\right\}}{\sum_k \left|P_\mathbf{r}^{(k)}\right|^2_{\mathrm{max}}}, \tag{5}$$

where $\mathbf{r}$ denotes the real-space coordinate vectors, respectively, and α denotes the weight coefficient for the $T_\mathbf{r}$ update.

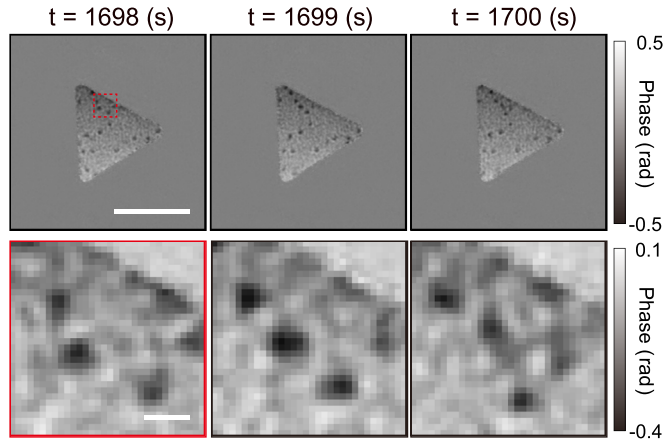

FIG. 3. Images of gold colloidal particles in an aqueous polyvinyl alcohol solution reconstructed from three consecutive diffraction patterns. The images below are magnified views of the areas enclosed by the red squares in the images listed above. The scale bar size in the upper image is 4 μm and 300 nm in the lower image.

The exit wave-field $\psi_\mathbf{r}^{(k)}$ and its Fourier transform $\widetilde{\Psi}_\mathbf{q}^{(k)}$ were determined as $\psi_\mathbf{r}^{(k)} = P_\mathbf{r}^{(k)} T_\mathbf{r}$ and $\widetilde{\Psi}_\mathbf{q}^{(k)} = \mathcal{F}[\psi_\mathbf{r}^{(k)}]$. Fifty iterations of phase-retrieval calculations were performed on each diffraction pattern using a weight coefficient of $\alpha = 0.6$. Figure 3 shows the object images reconstructed from three consecutive diffraction patterns with an exposure time of 1 s. The black dots represent colloidal gold particles. Some particles changed their positions over time. The motion of the particles can be displayed in the form of a video [34]. This video can be found in the Supplemental Material [34]. Although the image quality is poor compared with that shown in Fig. 3, we also reconstructed the object image with an exposure time of 0.1 s [34].

The SPT process, including single-particle detection and motion tracking, was then applied to the reconstructed images with an exposure time of 1 s to investigate the motion behavior of the particles [34]. Based on SPT results from CXDI frames, we estimated the diffusion coefficient D_{CXDI} for each particle by analyzing the mean-squared displacement (MSD) of the constructed trajectories [34]. Figure 4(a) shows the relationship between D_{CXDI} and the sampled period of time Δt using a linear regression model, where the dashed black line represents the linear correlation determined by the diffusion coefficient estimated from XPCS measurements. Figure 4(b) displays a histogram comparing the diffusion coefficients estimated from SPT on CXDI frames and XPCS.

In contrast to conforming to a Gaussian distribution centered around an expected value of a single diffusion coefficient, which typically implies a single type of diffusion [35], the distribution of the estimated diffusion coefficients displays a significant deviation. This deviation is characterized by a prominent peak on the left, corresponding to the low-value region, and several smaller peaks on the right, associated with the high-value region. These characteristics suggest instances of superdiffusion during which particles exhibit substantial displacements from their initial positions and subdiffusion during which particles are confined within

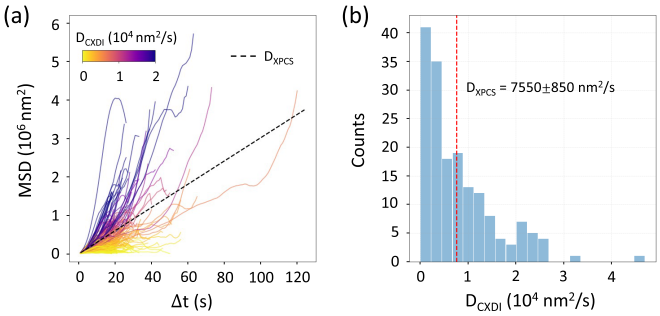

FIG. 4. (a) Diffusion coefficient D_{CXDI} estimated by fitting the mean-squared displacement (MSD) of particles tracked in coherent x-ray diffraction imaging (CXDI) frames with the sampled period of time Δt using a linear regression model. The dashed black line shows the linear dependence of MSD on the time interval according to the diffusion coefficient estimated from x-ray photon correlation spectroscopy (XPCS) measurements. (b) Histogram of the diffusion coefficients estimated by tracking single particles in CXDI frames and from XPCS measurements (red line).

limited areas. The visualization of these anomalous diffusion modes can be observed by considering the linear-fitting accuracy [34]. Notably, the average value of the diffusion coefficients D_{CXDI} estimated from tracking particles in CXDI frames is 8000 nm^2/s, which aligns with D_{XPCS} (7550 ± 850 nm^2/s), thus confirming the compatibility between the SPT process employed on CXDI frames and the XPCS experiments.

To gain a detailed understanding of the temporal evolution of motion modes, it is important to analyze trajectory segments rather than the entire trajectory, despite the overview provided by MSD analysis. To address this aspect, the sliding time window technique was used to convert each trajectory into fragments by shifting a time window of size w by a constant time step. Figure 5(a) shows a schematic deriving motion-related properties from a trajectory using the time-sliding window. Via defining the confined radii [7], two descriptors, tortuosity [8] and anisotropy, were introduced to respectively characterize the spatial extent and directionality of particle motion within each time window. The systematic investigation of the dependence of tortuosity and anisotropy on the time window size leads to Figs. 5(b) and 5(c), which respectively display the distributions of two descriptors captured by sliding time windows (with widths w) ranging from 20 to 40 frames and a fixed sliding time step of 5 frames in logarithmic axes. The tortuosity (σ_1^2/w) distributions predominantly exhibited single peaks when the sampling window width was between 20 and 25 frames, thus indicating translational motion along the σ_1 direction with an average speed of ≈1.4 pixels/s (56.8 nm/s). However, for $w \geqslant 30$ frames, a new peak emerged at $\sigma_1^2/w \approx 1$, suggesting back-and-forth motion patterns with an average speed of ≈ 1 pixels/s (40.6 nm/s). In terms of anisotropy (σ_2^2/σ_1^2), all estimated distributions displayed two peaks, thus representing directional and back-and-forth motions. As w increases, the contribution of the component with higher σ_2^2/σ_1^2 values increases, thus indicating that more particles comply with back-and-forth motion patterns at longer timescales. These findings for tortuosity and anisotropy consistently suggest the presence of at least two distinct modes associated with particle motion behavior.

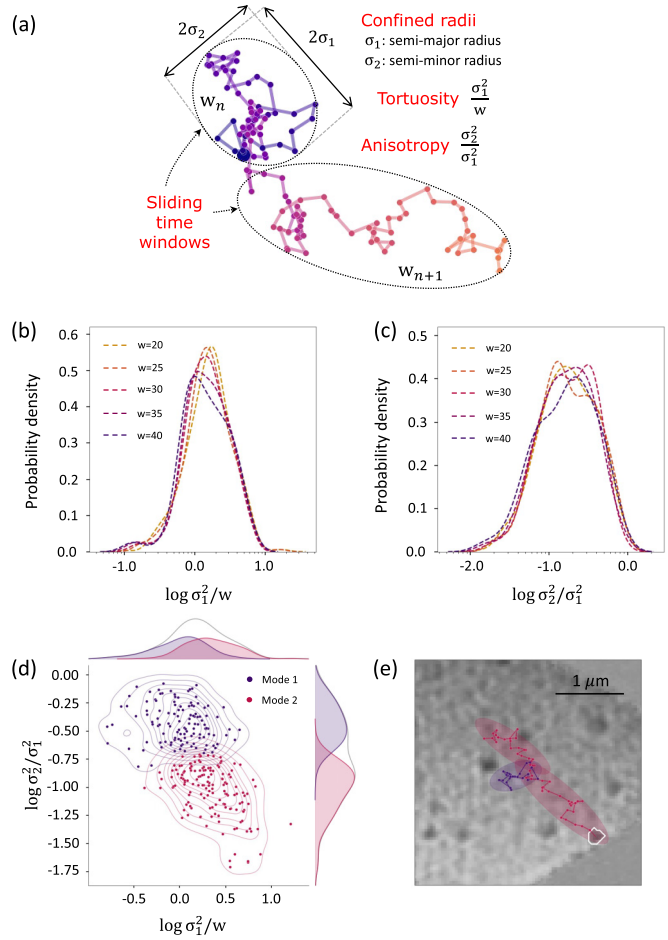

FIG. 5. (a) Schematic of deriving motion-related properties from a trajectory with a time-sliding window. (b, c) Distributions of (b) tortuosity and (c) anisotropy of trajectory fragments sampled by sliding windows of various widths with a constant step of 5 frames. (d) Joint distribution of the tortuosity and anisotropy of mode-assigned trajectory fragments sampled by overlapping time windows (width = 25 frames, step = 5 frames). (e) Trajectories of a particle experiencing different motion modes over time.

Further investigating the hypothesized behaviors of particle diffusion, we employed a joint distribution of the two descriptors sampled by an overlapped sliding window with a width of 25 frames and a sliding step of 5 frames, as shown in Fig. 5(d). A two-dimensional Gaussian mixture model with two components was applied to assign modes to all trajectory fragments based on tortuosity and anisotropy. From the joint distribution, and particularly in terms of anisotropy, these two modes of particle diffusion can be distinguished based on the characteristics of the trajectory fragments. Trajectory fragments categorized within the first mode, characterized by low logarithmic values of $\log(\sigma_1^2/w)$ and high logarithmic values of $\log(\sigma_2^2/\sigma_1^2)$, represent instances where particles diffuse with a low rate and no specific directional preference. Conversely, trajectory fragments assigned to the second mode, characterized by consistently high values of $\log(\sigma_1^2/w)$ and low values

of $\log(\sigma_2^2/\sigma_1^2)$, are indicative of particles displaying active diffusion along specific directions. Figure 5(e) shows an example of the trajectory of a single particle exhibiting different modes of motion and visually illustrates the discrimination between these modes. Indeed, the first mode can reasonably be attributed to simple Brownian motion and subdiffusion resulting from the confinement of particles within a narrow region, whereas the second mode likely corresponds to diffusive motion along a preferred direction (superdiffusion) [5,6]. Generally, particles in polymers can exhibit a variety of dynamic behaviors, including simple Brownian motion, subdiffusion, and superdiffusion [36,37]. In the present measured sample, a PVA solution, the presence of heterogeneity might influence particle motion, leading to the existence of multiple diffusive modes. Simple Brownian motion and subdiffusive motion were observed at short timescales and small spatial scales, while superdiffusive motion was observed at longer timescales and larger spatial scales. These distinct behaviors offer valuable insights into the heterogeneous dynamics of the solution over a substantial spatiotemporal scale [6,8,9], thereby highlighting novel aspects of particle diffusion within this specific context.

Our proposed measurement system and accompanying analysis of particle motions have the potential to offer a powerful tool to investigate the dynamic evolution of polymer materials and colloidal systems. XPCS provides an average depiction of the fast dynamics of particles. Conversely, dynamic CXDI provides a moving image of the slow motion of individual particles and uses a data-driven approach to analyze the mode of motion. Although XPCS in the ultrasmall-angle region allows access to dynamics at the micrometer range, quantitative evaluation is complex owing to the effects of multiple scattering [38]. Therefore, the current (combined) approach is promising for investigating the dynamics at microscopic scales and multiple modes of motion owing to various inhomogeneities at the macroscopic scale. For example, it can be applied to the analysis of nonexponential decay or multiple-step decay shapes of the time autocorrelation function [39], as well as the dynamic heterogeneity of various materials, such as polymer nanocomposites [40], glass-forming polymers [41], and magnetic colloidal systems [42].

The spatiotemporal resolution of this measurement method depends on the performance of the synchrotron radiation source and the imaging detector. With the advent of low-emittance synchrotron radiation sources and next-generation imaging detectors, further performance improvements are expected. Conversely, it should be noted that an increase in incident flux can cause non-negligible damage to the sample. This measurement method can also be applied to pump-probe CXDI measurements using free-electron lasers [43,44], where dynamics on the femtosecond-to-picosecond scale, which is difficult to measure with synchrotron radiation, can be analyzed. Currently, pump-probe CXDI is limited to isolated samples, and the present approach can be applied to spatially extended samples. We expect that this general approach can potentially allow imaging of a broad range of dynamical phenomena with high-spatiotemporal resolution.

This work was supported by the Japan Society for the Promotion of Science (JSPS) KAKENHI (Grants No. JP19H05814, No. JP20K15375, No. JP20K20523, No. JP22KJ0302, and No. JP23H05403). We thank Director Tetsuya Ishikawa of RIKEN SPring-8 Center for stimulating discussions.

[1] E. Manias, Stiffer by design, Nat. Mater. **6**, 9 (2007).
[2] D. Wirtz, Particle-tracking microrheology of living cells: Principles and applications, Annu. Rev. Biophys. **38**, 301 (2009).
[3] B. J. Berne and R. Pecora, *Dynamic Light Scattering: With Applications to Chemistry, Biology, and Physics* (Wiley, New York, 1976).
[4] H. Shen, L. J. Tauzin, R. Baiyasi, W. Wang, N. Moringo, B. Shuang, and C. F. Landes, Single particle tracking: From theory to biophysical applications, Chem. Rev. **117**, 7331 (2017).
[5] A. Kusumi, Y. Sako, and M. Yamamoto, Confined lateral diffusion of membrane receptors as studied by single particle tracking (nanovid microscopy): Effects of calcium-induced differentiation in cultured epithelial cells, Biophys. J. **65**, 2021 (1993).
[6] E. Parrish, M. A. Caporizzo, and R. J. Composto, Network confinement and heterogeneity slows nanoparticle diffusion in polymer gels, J. Chem. Phys. **146**, 203318 (2017).
[7] J. Lerner, P. A. Gomez-Garcia, R. L. McCarthy, Z. Liu, M. Lakadamyali, and K. S. Zaret, Two-parameter mobility assessments discriminate diverse regulatory factor behaviors in chromatin, Mol. Cell **79**, 677 (2020).
[8] J. J. E. Maris, F. T. Rabouw, B. M. Weckhuysen, and F. Meirer, Classification-based motion analysis of single-molecule trajectories using DiffusionLab, Sci. Rep. **12**, 9595 (2022).
[9] S. Kang, J. Kim, M. Lee, J. Yu, J. Kim, D. Kang, H. Baek, Y. Bae, B. Kim, S. Kang, S. Shim, S. Park, W. Lee, T. Hyeon, J. Sung, and J. Park, Real-space imaging of nanoparticle transport and interaction dynamics by graphene liquid cell TEM, Sci. Adv. **7**, eabi5419 (2021).
[10] O. G. Shpyrko, X-ray photon correlation spectroscopy, J. Synchrotron Radiat. **21**, 1057 (2014).
[11] F. Livet, F. Bley, F. Ehrburger-Dolle, I. Morfin, E. Geissler, and M. Sutton, X-ray intensity fluctuation spectroscopy by heterodyne detection, J. Synchrotron Radiat. **13**, 453 (2006).
[12] C. Klose, F. Büttner, W. Hu, C. Mazzoli, G. S. D. Beach, S. Eisebitt, and B. Pfau, Photon correlation spectroscopy with heterodyne mixing based on soft x-ray magnetic circular dichroism, Phys. Rev. B **105**, 214425 (2022).
[13] H. N. Chapman and K. A. Nugent, Coherent lensless X-ray imaging, Nat. Photonics **4**, 833 (2010).
[14] J. Miao, T. Ishikawa, I. K. Robinson, and Margaret M. Murnane, Beyond crystallography: Diffractive imaging using coherent x-ray light sources, Science **348**, 530 (2015).
[15] F. Pfeiffer, X-ray ptychography, Nat. Photonics **12**, 9 (2018).
[16] B. Abbey, K. A. Nugent, G. J. Williams, J. N. Clark, A. G. Peele, M. A. Pfeifer, M. de Jonge, and I. McNulty, Keyhole coherent diffractive imaging, Nat. Phys. **4**, 394 (2008).

[17] K. P. Khakurel, T. Kimura, H. Nakamori, T. Goto, S. Matsuyama, T. Sasaki, M. Takei, Y. Kohmura, T. Ishikawa, K. Yamauchi, and Y. Nishino, Generation of apodized X-ray illumination and its application to scanning and diffraction microscopy, J. Synchrotron Radiat. **24**, 142 (2017).

[18] F. Zhang, B. Chen, G. R. Morrison, J. Vila-Comamala, M. Guizar-Sicairos, and I. K. Robinson, Phase retrieval by coherent modulation imaging, Nat. Commun. **7**, 13367 (2016).

[19] Y. H. Lo, L. Zhao, M. Gallagher-Jones, A. Rana, J. J. Lodico, W. Xiao, B. C. Regan, and J. Miao, In situ coherent diffractive imaging, Nat. Commun. **9**, 1826 (2018).

[20] X. Tao, Z. Xu, H. Liu, C. Wang, Z. Xing, Y. Wang, and R. Tai, Spatially correlated coherent diffractive imaging method, Appl. Opt. **57**, 6527 (2018).

[21] G. N. Hinsley, C. M. Kewish, and G. A. van Riessen, Dynamic coherent diffractive imaging using unsupervised identification of spatiotemporal constraints, Opt. Express **28**, 36862 (2020).

[22] A. L. Levitan, K. Keskinbora, U. T. Sanli, M. Weigand, and R. Comin, Single-frame far-field diffractive imaging with randomized illumination, Opt. Express **28**, 37103 (2020).

[23] Y. Takayama, K. Fukuda, M. Kawashima, Y. Aoi, D. Shigematsu, T. Akada, T. Ikeda, and Y. Kagoshima, Dynamic nanoimaging of extended objects via hard X-ray multiple-shot coherent diffraction with projection illumination optics, Commun. Phys. **4**, 48 (2021).

[24] J. Kang, S. Takazawa, N. Ishiguro, and Y. Takahashi, Single-frame coherent diffraction imaging of extended objects using triangular aperture, Opt. Express **29**, 1441 (2021).

[25] S. Takazawa, J. Kang, M. Abe, H. Uematsu, N. Ishiguro, and Y. Takahashi, Demonstration of single-frame coherent X-ray diffraction imaging using triangular aperture: Towards dynamic nanoimaging of extended objects, Opt. Express **29**, 14394 (2021).

[26] K. Tamasaku, Y. Tanaka, M. Yabashi, H. Yamazaki, N. Kawamura, M. Suzuki, and T. Ishikawa, SPring-8 RIKEN beamline III for coherent X-ray optics, Nucl. Instrum. Methods Phys. Res., Sect. A **467-468**, 686 (2001).

[27] H. Eisenberg and E. H. Frei, Precision rotation viscometer with electrostatic restoring torque for the centipoise range, J. Polym. Sci. **14**, 417 (1954).

[28] E. H. R. Tsai, I. Usov, A. Diaz, A. Manzel, and M. Guizar-Sicairos, X-ray ptychography with extended depth of field, Opt. Express **24**, 29089 (2016).

[29] S. Berkowicz, S. Das, M. Reiser, M. Filianina, M. Bin, G. Crevatin, F. Hennies, C. Weninger, A. Björling, P. Bell, and F. Perakis, Nanofocused x-ray photon correlation spectroscopy, Phys. Rev. Res. **4**, L032012 (2022).

[30] O. Bikondoa and D. Carbone, X-ray photon correlation spectroscopy with coherent nanobeams: A numerical study, Crystals **10**, 766 (2020).

[31] M. Sutton, K. Laaziri, F. Livet, and F. Bley, Using coherence to measure two-time correlation functions, Opt. Express **11**, 2268 (2003).

[32] A. Danno, Gel formation of aqueous solution of polyvinyl alcohol irradiated by gamma rays from cobalt-60, J. Phys. Soc. Jpn. **13**, 722 (1958).

[33] Although the time range of Fig. 2(c) is not ideal to evaluate the shape of $g^{(2)}$, it is sufficient to evaluate $\Gamma(q)$ for a simple Brownian motion in the simple Newtonian fluid case.

[34] See Supplemental Material at http://link.aps.org/supplemental/10.1103/PhysRevResearch.5.L042019 for Video 1 with 1-s exposure and Video 2 with 0.1-s exposure, image of gold colloidal particles reconstructed from diffraction patterns obtained with 0.1-s exposure, and details of analysis techniques for performing SPT to extract and analyze the dynamics of individual particles; detection of single particles in CXDI frames, tracking particles for trajectory construction, results of particle detection and trajectory construction, and analysis of mean squared displacement, which also includes Ref. [5].

[35] T. Ragan, H. Huang, P. So, and E. Gratton, 3D particle tracking on a two-photon microscope, J. Fluoresc. **16**, 325 (2006).

[36] H. Guo, G. Bourret, R. B. Lennox, M. Sutton, J. L. Harden, and R. L. Leheny, Entanglement-controlled subdiffusion of nanoparticles within concentrated polymer solutions, Phys. Rev. Lett. **109**, 055901 (2012).

[37] T. Hoshino, D. Murakami, Y. Tanaka, M. Takata, H. Jinnai, and A. Takahara, Dynamical crossover between hyperdiffusion and subdiffusion of polymer-grafted nanoparticles in a polymer matrix, Phys. Rev. E **88**, 032602 (2013).

[38] E. F. Semeraro, J. Möller, and T. Narayanan, Multiple-scattering effects in SAXS and XPCS measurements in the ultra-small-angle region, J. Appl. Crystallogr. **51**, 706 (2018).

[39] M. Reiser, J. Hallmann, J. Möller, K. Kazarian, D. Orsi, L. Randolph, H. Rahmann, F. Westermeier, E. Stellamanns, M. Sprung, F. Zontone, L. Cristofolini, C. Gutt, and A. Madsen, Photo-controlled dynamics and transport in entangled wormlike micellar nanocomposites studied by XPCS, Macromolecules **55**, 8757 (2022).

[40] E. Senses, S. M. Ansar, C. L. Kitchens, Y. Mao, S. Narayanan, B. Natarajan, and A. Faraone, Small particle driven chain disentanglements in polymer nanocomposites, Phys. Rev. Lett. **118**, 147801 (2017).

[41] T. Hoshino, S. Fujinami, T. Nakatani, and Y. Kohmura, Dynamical heterogeneity near glass transition temperature under shear conditions, Phys. Rev. Lett. **124**, 118004 (2020).

[42] J. Lal, D. Abernathy, L. Auvray, O. Diat, and G. Grübel, Dynamics and correlations in magnetic colloidal systems studied by X-ray photon correlation spectroscopy, Eur. Phys. J. E **4**, 263 (2001).

[43] A. Barty, S. Boutet, M. J. Bogan, S. Hau-Riege, S. Marchesini, K. Sokolowski-Tinten, N. Stojanovic, R. Tobey, H. Ehrke, A. Cavalleri, S. Düsterer, M. Frank, S. Bajt, B. W. Woods, M. M. Seibert, J. Hajdu, R. Treusch, and H. N. Chapman, Ultrafast single-shot diffraction imaging of nanoscale dynamics, Nat. Photonics **2**, 415 (2008).

[44] Y. Ihm, D. H. Cho, D. Sung, D. Nam, C. Jung, T. Sato, S. Kim, J. Park, S. Kim, M. Gallagher-Jones, Y. Kim, R. Xu, S. Owada, J. H. Shim, K. Tono, M. Yabashi, T. Ishikawa, J. Miao, D. Y. Noh, and C. Song, Direct observation of picosecond melting and disintegration of metallic nanoparticles, Nat. Commun. **10**, 2411 (2019).